Field-dependent chemisorption of carbon monoxide and nitric oxide on platinum-group (111) surfaces: Quantum chemical calculations compared with infrared spectroscopy at electrochem…

4 AUTHORS, INCLUDING:

Marc Koper
Leiden University
302 PUBLICATIONS   9,198 CITATIONS

SEE PROFILE

Sally Wasileski
University of North Carolina at Asheville
24 PUBLICATIONS   981 CITATIONS

SEE PROFILE

Field-dependent chemisorption of carbon monoxide and nitric oxide on platinum-group (111) surfaces: Quantum chemical calculations compared with infrared spectroscopy at electrochemical and vacuum-based interfaces

Marc T. M. Koper[a)] and Rutger A. van Santen
Schuit Institute of Catalysis, Laboratory of Inorganic Chemistry and Catalysis, Eindhoven University of Technology, 5600 MB Eindhoven, The Netherlands

Sally A. Wasileski and Michael J. Weaver[a)]
Department of Chemistry, Purdue University, West Lafayette, Indiana 47907

Density Functional Theory (DFT) is utilized to compute field-dependent binding energies and intramolecular vibrational frequencies for carbon monoxide and nitric oxide chemisorbed on five hexagonal Pt-group metal surfaces, Pt, Ir, Pd, Rh, and Ru. The results are compared with corresponding binding geometries and vibrational frequencies obtained chiefly from infrared spectroscopy in electrochemical and ultrahigh vacuum environments in order to elucidate the broad-based quantum-chemical factors responsible for the observed metal- and potential-dependent surface bonding in these benchmark diatomic chemisorbate systems. The surfaces are modeled chiefly as 13-atom metal clusters in a variable external field, enabling examination of potential-dependent CO and NO bonding at low coverages in atop and threefold-hollow geometries. The calculated trends in the CO binding-site preferences are in accordance with spectral data: Pt and Rh switch from atop to multifold coordination at negative fields, whereas Ir and Ru exhibit uniformly atop, and Pd hollow-site binding, throughout the experimentally accessible interfacial fields. These trends are analyzed with reference to metal *d*-band parameters by decomposing the field-dependent DFT binding energies into steric (electrostatic plus Pauli) repulsion, and donation and back-donation orbital components. The increasing tendency towards multifold CO coordination seen at more negative fields is due primarily to enhanced back-donation. The decreasing propensity for atop vs multifold CO binding seen in moving from the lower-left to the upper-right Periodic corner of the Pt-group elements is due to the combined effects of weaker donation, stronger back-donation, and weaker steric repulsion. The uniformly hollow-site binding seen for NO arises from markedly stronger back-donation and weaker donation than for CO. The metal-dependent zero-field DFT vibrational frequencies are in uniformly good agreement with experiment; a semiquantitative concordance is found between the DFT and experimental frequency-field (''Stark-tuning'') slopes. Decomposition of the DFT bond frequencies shows that the redshifts observed upon chemisorption are due to donation as well as back-donation interactions; the metal-dependent trends, however, are due to a combination of several factors. While the observed positive Stark-tuning slopes are due predominantly to field-dependent back-donation, their observed sensitivity to the binding site and metal again reflect the interplay of several interaction components. © *2000 American Institute of Physics.* [S0021-9606(00)70234-0]

I. INTRODUCTION

As for metal surfaces in ultrahigh vacuum (UHV) or gas-phase environments, carbon monoxide and nitric oxide constitute chemisorbates of particular significance in metal-solution (i.e., electrochemical) systems. The establishment of infrared reflectance-absorption spectroscopy (IRAS) as a sensitive *in situ* vibrational probe of electrochemical interfaces, along with now-reliable means of preparing ordered monocrystalline surfaces in these environments, has over the past decade yielded increasingly detailed information on chemisorbate structure, bonding, and reactivity.[1] The Purdue

group, among others, has been utilizing electrochemical IRAS to examine CO and NO chemisorption at monocrystalline Pt-group metal-solution interfaces.[2–8] The extensive microscopic structural information available for the corresponding UHV-based systems from a number of techniques, including IRAS, enable uniquely detailed intercomparisons of chemisorbate properties in electrochemical and UHV environments.[8]

While the electrochemical interfaces are structurally more complex, necessarily containing solvent and electronic/ ionic charges, they provide intriguing opportunities to examine the effects of high (up to $\approx 10^8$ V cm^{-1}) and variable electrostatic fields on chemisorbate bonding. Indeed, the electrochemical infrared spectra for chemisorbed CO and

---

[a)]Authors to whom correspondence should be addressed.

NO are sensitive to the applied electrode potential, displaying marked shifts in the intramolecular stretching frequencies and in some cases indicating alterations in the chemisorbate binding sites.[2–5,8] Unlike the complex influences of coadsorbed charge observed for solvent-free UHV-based systems, the potential-dependent chemisorbate infrared spectra for the electrochemical interfaces indicate the occurrence of nonspecific electrostatic effects upon the surface bonding.[9,10] The central importance of the surface potential (and hence electrostatic field) in modifying the surface bonding is indicated further from the near-concordance (within $10–20$ cm^{-1}) of the chemisorbate vibrational frequencies for corresponding electrochemical and UHV-based systems when the former are evaluated at electrode potentials equivalent to the work functions (and hence surface potentials) measured for the latter interfaces.[8,9]

The theoretical understanding of chemisorbate bonding on transition metals has been advanced notably by the application of Density Functional Theory (DFT) using metal clusters and slabs as model surfaces.[11,12] This approach has been shown to yield binding-site energetics and vibrational frequencies for chemisorbed CO and NO on some Pt-group surfaces that are in reasonable concordance with UHV-based experimental results.[12–14] Significantly, the DFT results provide a detailed quantum-chemical description of the chemisorbate bonding. Given these developments, it is of considerable interest to develop also a quantum-chemical picture of electrostatic field effects on surface bonding, of relevance to electrochemical systems and other situations (e.g., ionic or dipolar coadsorption) where the interfacial field is varied. There have been several previous studies along these general lines, using semiempirical as well as *ab initio* theoretical approaches.[15–20] Two of us have recently undertaken initial DFT cluster calculations examining the effects of electrostatic field upon CO and NO chemisorption in atop and threefold-hollow sites on Pt(111).[20] The findings provide a quantum-chemical rationalization of several experimental findings, including the increasing preference for multifold CO binding on Pt(111) towards more negative electrode potentials, and the greater electrode-potential dependence of NO vs CO stretching frequencies.[20]

An interesting yet largely unexplored issue is understanding how the electrostatic field-dependent chemisorbate bonding varies across the Pt-group metals. Indeed, theoretical examinations of the marked variations in CO coordination geometry observed experimentally between these surfaces, even at zero external field, are relatively sparse.[21] To this end, the present paper reports DFT calculations for CO and NO chemisorption on the four Pt-group (111) surfaces— platinum, iridium, palladium, and rhodium, as well as on the related hexagonal Ru(0001) surface—for which potential-dependent IRAS data, along with detailed results for the UHV-based interfaces, are available. We undertake a broad-based comparison of the DFT results with the experimental findings, focusing attention on the quantum-chemical factors responsible for the observed variations in the preferred binding site and the vibrational frequencies with the metal surface, chemisorbate, and electrostatic field. Taken together, the DFT predictions of binding energies and intramolecular vibrational frequencies for the chemisorbed CO and NO not only account reasonably well for the experimental trends, but, more significantly, provide detailed insight into the field-dependent nature of chemisorbate bonding.

II. COMPUTATIONAL METHODS

Most calculations reported here made use of a 13-atom cluster model of the (111) surfaces, arranged in two hexagonal layers of 6 and 7 atoms. The same arrangement also provides a model of the Ru(0001) surface. The CO and NO molecules were adsorbed in the upright position, so that all clusters possess C_{3v} symmetry, with the C and N closest to the metal plane. The 7-atom layer provides the atop adsorption site, whereas the opposite 6-atom surface provides the (hcp) hollow geometry. (Note that the difference in calculated CO and NO adsorption energy for the hcp and fcc hollow adsorption sites is generally small, on the order of 0.05 eV; see, e.g., Refs. 13 and 14.) The provision of the intermediate two-fold bridging geometry site, although of experimental interest, requires greater computational time due to the lowered cluster symmetry and was not pursued in the present calculations. Due to convergence problems with Rh_{13}, calculations for this metal utilized instead a two-layer $(7,3)Rh_{10}$ cluster for atop binding, and a three-layer $(6,7,3)Rh_{16}$ cluster for the hollow site.

Using a cluster model to describe an extended surface has well-documented disadvantages.[11] At best, they can be considered reasonable for low adsorbate coverages, provided an assessment is made of the effects of finite cluster size. However, the DFT cluster model is well suited to the broad survey undertaken here, being computationally much less demanding than those based on a periodic slab approach. Furthermore, like equilibrium bond distances, vibrational properties depend on the gradient of the potential energy, for which the cluster approach is found to be reasonably accurate. We briefly discuss the cluster size effect and make a comparison to available slab calculations below.

All results reported here have been obtained with the Amsterdam Density Functional (ADF) Package.[22–24] Slater-type orbitals are used to represent the atomic orbitals. To enhance computational efficiency, the innermost atomic shells of all atoms are kept frozen, as these core electrons do not contribute significantly to the chemical bonding. The extent of these frozen cores was up to and including the following orbitals: C $1s$, N $1s$, O $1s$, Ru $4p$, Rh $4p$, Pd $4p$, Ir $5p$, Pt $5p$. The Ru, Rh, Pd, Ir, and Pt basis sets were of double-ζ quality; in addition, the C, N, and O basis sets were augmented by polarization functions. The Kohn–Sham one-electron equations were solved in the so-called DFT-GGA approximation.[25] The Vosko–Wilk–Nusair[26] form of the local density approximation was used, in combination with the BP86 functional[27] for the generalized gradient approximation (GGA). Relativistic effects within the cores were accounted for self-consistently by first-order perturbation theory. All cluster calculations were carried out in the spin-restricted mode. The energy of the bare NO molecule, however, was obtained in the spin-unrestricted mode, as NO has one unpaired electron in the $2\pi^*$ orbital. The effect of altering the

TABLE I. Potential-dependent binding sites for CO and NO on Pt-group (111) surfaces.

Phase[a]	Low coverage[c] Φ, eV[b]		Saturated coverage[d] Φ, eV[b]		Phase	Low coverage[c] Φ, eV[b]		Saturated coverage[d] Φ, eV[b]	
		Rh(111)/CO					Pd(111)/CO		
UHV	5.5	atop[e]	6.2	atop/hollow (2×2)[s]	UHV	5.6	hollow	~6.6	atop/hollow (2×2)[k]
EC	>5.0	atop[f]	>5.0	atop/hollow (2×2)[g]	EC	4.8–5.4	hollow	4.8–5.4	bridging/hollow?[l]
	<5.0	bridge[f]	<4.8	multifold[g]					
		Rh(111)/NO					Pd(111)/NO		
UHV	5.5	hollow	~5.5	atop/hollow (2×2)[h]	UHV	5.6	hollow	~5.6	atop/hollow?[m]
EC	5.0–5.6	hollow	>5.5	atop/hollow (2×2)[h]	EC	4.8–5.5	?	4.8–5.5	atop?[n]
		Ir(111)/CO					Pt(111)/CO		
UHV	5.7	atop	5.9	atop	UHV	5.9	atop[o]	6.0	atop/bridge[o]
EC	4.8–5.3	atop	4.8–5.3	atop	EC	>5.2	atop[f]	>5.2	atop/bridge[p]
		Ir(111)/NO					Pt(111)/NO		
UHV	5.7	?[j]	~5.8	atop?[j]	UHV	5.9	hollow[g]	5.8	hollow[q]
EC	5.0–5.6	?[j]	5.0–5.6	atop?[j]	EC	5.0–5.6	hollow[r]	5.0–5.6	hollow[r]

[a]UHV=ultrahigh vacuum, EC=aqueous electrochemical environment.

[b]Work function of interface. ''Low-coverage'' UHV-based values are for clean metal surfaces, and ''saturated-coverage'' values include effect of adlayer. Values taken from Ref. 8, where literature sources are also listed. Values of Φ for electrochemical interfaces refer to range over which IRAS (and in some cases STM) measurements adlayer structure have been determined. They were obtained from measured electrode potentials, presuming that the ''absolute potential'' of the SHE is 4.8 V (see text and Ref. 8).

[c]Refers to sufficiently low adsorbate coverages (usually <20% of saturation) so that only energetically preferred binding site is occupied. Evidence for preferred binding sites from Ref. 8(b), and/or from references cited for specific systems.

[d]Refers to saturated (or near-saturated) adsorbate coverages, where compressed adlayers are formed. Evidence for binding sites from Ref. 8, and/or from reference cited. ''(2×2)'' refers to (2×2)-3CO or (2×2)-3NO adlayers ($\theta=0.75$) containing two hollow and one atop molecules per unit cell.

[e]Reference 22.

[f]Reference 2(b).

[g]Structures determined by *in situ* STM [Ref. 5(a)]. Reassignment of high-potential (2×2) structure to atop/hollow coordination prompted by revised LEED analysis of corresponding UHV-based system (Ref. 22), along with concordance of EC/UHV ν_{CO} values at equivalent surface potentials [Ref. 8(a)], indicating structural similarity of the EC system. Low-potential structure dominated by bridging/hollow coordination as deduced from IRAS/STM data [Ref. 5(a)].

[h]From photoelectron diffraction analysis for UHV systems (Ref. 31). Likely structural similarity of saturated coverage EC adlayer at $\Phi \geqslant 5.5$ eV indicated from near-equivalent IRAS behavior [Ref. 8(a)].

[i]Binding-site uncertainties at low NO coverages caused by nonavailability of UHV-based data, and NO island formation in the EC system [Ref. 7(c)].

[j]Possible atop NO coordination suggested by high-frequency ($\sim$1830–1870 cm^{-1}) ν_{NO} values in UHV and EC environments [Ref. 8(a)].

[k]From photoelectron diffraction [Ref. 29(b)].

[l]Suggested from EC-IRAS data (Ref. 32).

[m]Reinterpretation of IRAS data, suggested by recent DFT calculations [Ref. 13(b)].

[n]Prevalent atop coordination in the EC system suggested by the high-frequency ($\sim$1750 cm^{-1}) ν_{NO} band [Ref. 8(a)]

[o]Reference 33.

[p]As deduced from IRAS/STM [Ref. 5(b)]. Additional potential-induced hollow-bridging CO interconversion, as deduced by IRAS (Ref. 34).

[q]From tensor LEED analysis [Ref. 29(a)].

[r]Similar hollow-site preference for EC as for UHV system indicated by near-equivalent coverage-dependent ν_{NO} values (Ref. 8).

[s]Reference 30.

electrode potential was modeled by applying a variable external electric field F, in V/Å, across the cluster.

The C–O and N–O stretching frequencies were calculated using the ANHARMND program,[28] from a potential-energy surface consisting of 9–11 points for displacements of ca. ± 0.2 Å from the equilibrium bond length. This relatively wide range ensures that we obtain a reasonable description of the first vibrational excited state and possible anharmonic contributions. The potential-energy surface for the chemisorbate intramolecular bond was obtained by fixing the molecule's center of mass at its equilibrium position. This procedure to effectively decouple the internal stretching from the substrate-molecule vibration is approximately valid since the latter has a considerably (5–10-fold) lower frequency.[19]

III. RESULTS AND DISCUSSION

A. Experimental findings

As a prelude to discussing the DFT results, we present a brief overview of the site-selective adsorbate binding as deduced experimentally by IRAS and other means for the eight chemisorbate–metal combinations of interest here, including their sensitivity to the surface potential, along with the observed potential-dependent vibrational frequencies.

Table I provides a summary of the preferred binding sites obtained for CO and NO on the four (111) surfaces of concern here. As is conventional, the designations ''atop,'' ''bridge,'' and ''hollow,'' refer to binding CO and NO chemisorbates (via the C and N atoms) to one, two, or three metal atoms, respectively, on the (111) plane. Results are

given for both low and saturated (or near-saturated) coverages, and in UHV and aqueous electrochemical (EC) environments. Work functions (Φ, eV) measured for the former interfaces are listed, along with the corresponding values for which IRAS (or other) measurements were made for the electrochemical systems. This common, vacuum-based, ''surface potential'' scale is employed here for the UHV and EC interfaces for convenience. The Φ values for the latter are converted from the measured electrode potentials by presuming that the ''absolute potential'' of the standard hydrogen electrode (SHE) is 4.8 V. (This value was shown recently to yield a close concordance between potential-dependent EC and UHV-based chemisorbate vibrational frequencies.[8]) Since the UHV-based interfaces are necessarily charge-/solvent-free, the Φ values correspond to zero *external* applied field, $\Phi(F=0)$. Note that the accessible electrode potentials for the aqueous electrochemical systems span a range of values up to $\approx$ 1–1.5 V below this ''zero field'' condition, thereby corresponding to *negative F* values (i.e., where the metal surface acquires excess electronic charge).

The strategies used to determine the chemisorbate binding sites are given in the footnotes to Table I, along with cited references. The limitations of employing ''characteristic'' vibrational frequencies for adsorbed CO and, especially, NO for determining binding site geometries are now well-documented.[29] In particular, the typical preference of NO for hollow-site binding on late transition metals has been clarified on the basis of photoelectron diffraction,[29(a),29(b)] tensor low-energy electron diffraction (LEED) measurements,[29(c)] and DFT calculations.[13] Nevertheless, the vibrational spectral fingerprints *taken together* with the latter information can now yield reliable binding-site assignments for most of the present systems. While electron-diffraction measurements are clearly inapplicable to *in situ* electrochemical systems, relatively direct binding-site arrangements have been obtained for some saturated CO adlayers by combining IRAS data with scanning tunneling microscopy (STM) measurements.[5] In addition, reliable binding-site information for the majority of the electrochemical interfaces can be obtained by matching the intramolecular stretching frequencies for CO and NO, ν_{CO} and ν_{NO}, respectively, to the corresponding values measured for the UHV-based systems at ''equivalent surface potentials,'' [8] as outlined below.

For convenience, a summary of stretching frequencies obtained for eight metal/adsorbate combinations in the UHV and aqueous electrochemical environments is given in Table II. As in Table I, data are included for both low and saturated coverages. For each surface, ν_{CO} and ν_{NO} values are listed for the UHV and EC systems [(labeled ν(UHV) and ν(EC))] at electrode potentials for the latter corresponding to the work functions $\Phi(F=0)$ measured for the former (cf. Ref. 8). These ''equivalent surface potential'' ν(UHV) and ν(EC) values are seen to be in good agreement in most cases, reflecting a dominant influence of the surface potential (and hence the interfacial field) on the stretching frequencies. An exception is the Pd(111)/NO system, where the markedly ($\approx$ 150 cm^{-1}) higher EC ν_{NO} value at low coverages probably reflects a specific influence of coadsorbed solvent in

altering the NO binding geometry.[8(b)] Also listed for each EC system in Table II are the measured ''Stark tuning slopes'' $d\nu/dE$. One focus of the DFT results considered below is the comparison of these quantities with the calculated dependence of stretching frequencies on the external field.

Examination of the binding-site preferences in Table I reveals some interesting trends. The propensity for CO atop vs multifold coordination at low coverages increases in the sequence Pd<Pt$\sim$Rh<Ir. In addition, CO binding is exclusively atop on Ru(0001) in UHV,[36] even though electrochemical coverage-dependent data are not yet available. While atop CO coordination is also preferred on Pt, Rh, and Ir at zero external field under these conditions, the first two metals switch to multifold (bridge) coordination at negative fields, corresponding to Φ values more than $\approx$1.0 and 0.5 eV below $\Phi(F=0)$, respectively. For Ir and Pd, atop and multifold (hollow-site) coordination, respectively, is preferred throughout the accessible potential range. For saturated CO coverages at $F\approx0$, however, Rh(111) as well as Pd(111) surfaces yield the (2×2)-3CO configuration, containing a pair of hollow-site and a single atop CO per unit cell. The presence of negative fields at the EC interfaces triggers multifold binding, although the (2×2)-3CO adlayer is maintained on rhodium until Φ-$\Phi(F=0)\approx-1.0$ eV (Table I). This increasing propensity for multifold CO binding for negative fields is also evident for saturated adlayers on Pt(111), where the same (2×2)-3CO configuration is stable at lower electrode potentials.[5(b)] Consistent with the low-coverage trends noted above, exclusive atop CO coordination is evident on Ir(111) even at high coverages, and throughout the accessible electrode potential range, corresponding to Φ-$\Phi(F=0)$ values down to ca -1.0 eV.

While the metal-dependent trends in NO coordination geometry are less clear-cut, hollow-site binding is evidently present to a markedly greater extent than is the case for CO (Table I). Thus hollow NO coordination is preferred even at $\Phi(F=0)$ at low coverages on both Rh(111) and Pt(111), which is maintained at negative external fields in the EC environments. However, the Pd(111)/NO system is somewhat anomalous in this regard; while hollow coordination is obtained at low coverages in UHV, higher ν_{NO} values are obtained at the electrochemical interface (Table II), suggestive of bridging or even atop NO binding.[8(a)] As mentioned above, this behavior probably reflects a specific influence of coadsorbed solvent.[8(b)] The binding geometries in the Ir(111)/NO system are also uncertain. The high ν_{NO} values ($\approx$ 1850 cm^{-1}) observed in the UHV and EC environments (Table II) is suggestive of atop rather than multifold coordination.[8] We will consider this issue further below, in comparison with the DFT results.

The observed trends in the Stark-tuning slopes ($d\nu/dE$) summarized in Table II are also worth noting briefly here, even though they have been previously described.[4,8(a)] First, the slopes generally decrease towards higher coverages, the values for saturated adlayers typically being 1.5–2-fold smaller than for dilute adsorbates. Second, multifold CO coordination tends to yield larger Stark-tuning slopes than for atop CO. Third, the values for NO are typically larger (by 1.5–3-fold) than for CO in the same coordination geometry

TABLE II. Potential-dependent stretching frequencies for CO and NO on Pt-group (111) surfaces.

System	Coverage[a]	Φ[b] eV	ν(UHV)[c] cm^{-1}	ν(EC)[d] cm^{-1}	$d\nu/dE$[e] cm^{-1} V^{-1}	Binding[f] site
Pt/CO	low	5.9	2084[g]	2082	40	atop
	sat	6.0	2105/1855[g]	2100/1905[h]	30/45[h]	atop/bridge
	sat	6.0		2090/1835[i]	25/45[i]	atop/hollow
Pt/NO	low	5.9	$\approx$1700/1500[j]	1700/1480[j]	85/85	hollow
	sat	5.8	1714	1712	60	hollow
Ir/CO	low	5.7	2045	2055	50	atop
	sat	5.85	2090	2092	25	atop
Ir/NO	sat	5.8	1860	1865	60	atop?
Pd/CO	low	5.6	~1830	~1870	~50	hollow
Pd/NO	low	5.6	~1560	(1720)[k]	(35)[k]	hollow
Rh/CO	low	5.4	2020	2030	~40	atop
	sat	~6.1	2065/1855[l]	2070/1855[m]	30/45[m]	atop/hollow
Rh/NO	low	5.4	1520	~1540	120	hollow
	sat	~5.5	1840/1635[n]	1825/1600[o]	80[p]	atop/hollow

[a]"low" denotes coverages below $\approx$20% of saturation value; "sat" refers to saturated (or near-saturated) compressed adlayers.

[b]Work function of solvent/charge-free UHV interface; values for saturated adlayers include adsorbate-induced Φ change. See Ref. 8 for data sources, etc.

[c]Intramolecular stretching frequencies for CO or NO in the solvent/charge-free UHV environment. Taken from literature sources given in Ref. 8, except where noted.

[d]As (*c*), but in aqueous electrochemical environment at electrode potentials equivalent to work function of corresponding UHV-based interface. (See text and Ref. 8 for details.)

[e]Dependence of CO or NO stretching frequency on electrode potential. See Ref. 8 for literature sources, except where noted.

[f]Chemisorbate binding site (see Table I and Ref. 8 for data sources).

[g]Reference 35.

[h]EC-IRAS data corresponding to atop/bridge ($\theta_{CO}\approx$0.7) structure, seen at high potentials for saturated CO adlayers [Refs. 2(b) and 5(b)].

[i]EC-IRAS data [from Refs. 5(b) and 26] corresponding to the atop/hollow (θ_{CO}=0.75) structure [Ref. 5(b)].

[j]Both higher- and lower-frequency ν_{NO} bands seen at low NO coverages correspond to hollow-site adsorption apparently associated with bent and upright NO orientations, respectively on the basis of NEXAFS data (Ref. 35) [see Ref. 8(b)].

[k]Parentheses denote that higher ν_{NO} values for EC system suggest occurrence instead of preferred atop binding [see Table I and Ref. 8(b)].

[l]Vibrational frequencies for (2×2)-3CO LEED structure (θ_{CO}=0.75), corresponding to atop/hollow-site adsorption.

[m]Corresponding to (2×2)-3CO structure (θ_{CO}=0.75) deduced by STM [Ref. 5(a)], with structural reassignment to atop/hollow-site adsorption (see footnote g of Table I).

[n]Vibrational frequencies corresponding to (2×2)-3NO structure (θ_{NO}=0.75), now known to feature atop/hollow-site binding (Ref. 31) [cf. Rh(111)/CO structure].

[o]High-potential EC-IRAS fingerprint corresponding to the (2×2) structure in UHV [see Ref. 8(a)].

[p]For hollow-site NO at high coverages [Ref. 8(a)].

and coverages. The latter two trends are discussed below in comparison with the field-dependent DFT results.

B. Computational results and comparisons with experiment

1. Zero-field binding energies

Tables III and IV give the binding energies, E_b, obtained for CO and NO, respectively, adsorbed in the atop and hollow site of the Ru, Rh, Pd, Ir, and Pt clusters at zero external field. (Note that the metals are arranged in Periodic fashion.) The energy difference for the atop vs threefold hollow binding, ΔE_b, is also given in Table III and IV, such that negative and positive values imply preferential chemisorption in the former and latter geometries, respectively. (More negative E_b values correspond to stronger surface–chemisorbate binding.) The binding energies were obtained

with the CO and NO bond lengths at their coordinated equilibrium values (Tables III and IV), obtained from the potential energy-bond displacement minima.

Our chemisorbate binding energies are typically smaller (less negative) than the available periodic slab results,[12–14,37] but not far from experimental values.[38] Apart from cluster size effects, the absolute discrepancies between the E_b values extracted from cluster and periodic slab calculations have two main origins. First, we do not allow for a surface relaxation of the metal atoms. Secondly, however, most available slab calculations are based on the PW91 GGA-functional,[13,14] which is known to yield adsorption energies for CO and NO on transition-metal surfaces that are larger than experiment.[39] A better GGA functional can alter the calculated binding energies by as much as 0.5–0.7 eV, yielding results closer to experiment.[39] The BP86 functional used in this study yields somewhat lower binding energies than does PW91.[36,39] Nevertheless, our cluster calculations and the

TABLE III. Metal-dependent CO binding parameters at zero external field.[a]

	Ru			Rh			Pd	
	Atop	Hollow		Atop	Hollow		Atop	Hollow
r_{M-C}/Å	1.92	1.58	r_{M-C}/Å	1.86	1.47	r_{M-C}/Å	1.96	1.61
r_{C-O}/Å	1.165	1.199	r_{C-O}/Å	1.162	1.182	r_{C-O}/Å	1.160	1.176
E_b/eV	−1.18	−0.94	E_b/eV	−1.46	−1.36	E_b/ev	−0.91	−1.15
E(st)/eV	5.77	4.15	E(st)/eV	6.80	7.27	E(st)/eV	0.59	−0.82
E(orb)/eV	−6.95	−5.09	E(orb)/eV	−8.26	−8.62	E(orb)/eV	−1.50	−0.33
ΔE_b/eV	−0.24		ΔE_b/eV	−0.10		ΔE_b/eV	0.24	

		Ir			Pt	
		Atop	Hollow		Atop	Hollow
CO	r_{M-C}/Å	1.88	1.63	r_{M-C}/Å	1.90	1.52
	r_{C-O}/Å	1.160	1.189	r_{C-O}/Å	1.154	1.191
	E_b/eV	−1.40	−1.06	E_b/eV	−1.15	−1.20
	E(st)/eV	9.54	7.08	E(st)/eV	7.79(9.70)	5.90(11.95)
	E(orb)/eV	−10.95	−8.14	E(orb)/eV	−8.64	−6.38
	Δ_b/eV	−0.34		ΔE_b/eV	0.05	

[a]r_{M-C} and r_{C-O} are the equilibrium metal–CO and C–O bond distances, respectively; E_b is the total binding energy; E(st) and E(orb) are the steric repulsion and total orbital contributions to E_b; ΔE_b is the difference between the binding energies in the atop vs hollow site. Values of E(st) given for Pt/CO in parentheses are ''bond-constrained'' quantities, calculated with r_{C-O} *constrained* to equal the calculated bond length in the uncoordinated state, 1.139 Å (see text).

available slab results are in reasonable concordance with respect to the ΔE_b values, i.e., the energetic site preference, which is of primary interest here.

While the E_b values given in Tables III and IV refer to the 13-atom cluster geometry noted above (except for Rh), we typically found comparable binding energies and binding-site preferences on larger clusters. Nonetheless, altering the number of atoms in the first metal plane can influence the relative binding-site energies. For example, for (12, 6, 7) rhodium and iridium M_{25} clusters, the hollow site (on the 12-atom layer) is preferred for CO, contrasting the finding for the smaller clusters (Table III). [The latter, not the former, is in accordance with experiment (Table I).] However, when 6 atoms from the 12-atom layer in the 25(12, 6,

7) clusters were transferred to the other surface layer which accommodates the atop adsorption site, making a 25(6, 6, 13) geometry, the CO binding-site preference for both metals reverted to atop. Apparently, then, the number of surface layer atoms should be comparable in order to get a ''realistic binding-site'' estimation. Analysis of the ADF output showed that the importance of back-donation to the chemical bonding increases with a higher number of surface-layer atoms.

Of central interest here is understanding the factors influencing the variations on the preferred binding-site energies between the five Pt-group metals, initially at zero external field, as summarized in Tables III and IV. Significantly, inspection of the ΔE_b values for CO binding in Table III

TABLE IV. Metal-dependent NO binding parameters at zero external field.[a]

	Ru			Rh			Pd	
	Atop	Hollow		Atop	Hollow		Atop	Hollow
r_{M-N}/Å	1.82	1.54	r_{M-N}/Å	1.83	1.56	r_{M-N}/Å	1.96	1.42
r_{N-O}/Å	1.188	1.220	r_{N-O}/Å	1.191	1.216	r_{N-O}/Å	1.164	1.193
E_b/eV	−1.63	−2.05	E_b/eV	−1.68		E_b/eV	−1.13	−2.27
E(st)/eV	7.29	3.27	E(st)/eV	5.89		E(st)/eV	3.36	1.62
E(orb)/eV	−8.92	−5.32	E(orb)/eV	−7.56		E(orb)/eV	−4.49	−3.88
ΔE_b/eV	0.42		ΔE_b/eV			ΔE_b/eV	1.14	

		Ir			Pt	
		Atop	Hollow		Atop	Hollow
NO	r_{M-N}/Å	1.85	1.63	r_{M-N}/Å	1.94	1.53
	r_{N-O}/Å	1.181	1.211	r_{N-O}/Å	1.168	1.206
	E_b/eV	−1.23	−1.98	E_b/eV	−0.49	−1.70
	E(st)/eV	9.07	4.38	E(st)/eV	7.37	4.30
	E(orb)/eV	−10.30	−6.36	E(orb)/eV	−7.56	−5.70
	ΔE_b/eV	0.75		ΔE_b/eV	1.21	

[a]As in Table III, except that r_{M-N} and r_{N-O} are the equilibrium metal–NO and N–O bond distances. Values omitted for Rh/NO hollow due to unsatisfactory data convergence.

TABLE V. Orbital contributions (eV) to the CO and NO binding energies at zero external field in a "bond-prepared state."

Metal	A_1 (donation)	E (back-donation)	A_1 (donation)	E (back-donation)
	CO atop		CO hollow	
Ru	−3.84	−2.98	−1.33*	−3.91*
Rh	−5.36*	−2.98*	−3.87*	−4.63*
Pd	0.24	−1.71	1.91	−2.34
Ir	−7.14	−3.64	−2.42*	−5.32*
Pt	−5.86*	−3.10*	−2.20*	−4.71*
	NO atop		NO hollow	
Ru	−3.35	−5.29	0.76*	−6.10*
Rh	−2.47*	−4.53*	···	···
Pd	−0.88	−3.33	1.98	−5.95
Ir	−4.90	−4.89	0.21*	−6.41*
Pt	−4.52*	−3.11*	−0.29*	−5.91*

*These states are for the ground state [metal+CO/NO] cluster energy referred to an *excited-state* bare cluster, such that the difference in orbital occupations between the ligated and bare metal cluster is $a_1^6 e^4$ and $a_1^6 e^5$, for CO and NO, respectively (for explanation, see text). Values for Rh/NO hollow omitted due to unsatisfactory data convergence.

reveal a broad agreement with the experimental observations (Table I), which show a decreasing preference for atop binding in the sequence Ru~Ir<Rh~Pt<Pd. The observed preference instead for CO hollow-site binding on the last metal is also mimicked by the calculational findings (Table III). For NO, the uniform preference for hollow-site adsorption predicted by DFT (Table IV) is largely in harmony with experiment (Table I), with the apparent exception of iridium (vide infra).

In order to understand these variations, it is useful to decompose the computed binding energies into their major components, similarly to that undertaken in a previous paper.[20] These are the steric portion of the binding energy (comprising the Pauli repulsion and electrostatic parts) and the molecular-orbital terms. The total steric and orbital components of E_b, labeled $E(\text{st})$ and $E(\text{orb})$, are also listed for each metal-chemisorbate geometry in Tables III and IV. The latter contribution can in principle also be decomposed into components from the different irreducible representations of the symmetry point group. The relevant orbital components here for the C_{3v} symmetry cluster, are the A_1 (σ) and $E(\pi)$ terms, corresponding to donation and back-donation, respectively.

This further orbital decomposition, however, is in a sense ambiguous as the values depend on the electronic configuration of the corresponding bare cluster ground state. The electronic ground state of uncoordinated CO is $a_1^6 e^4$. When CO binds to the metal cluster, often 6 electrons from CO reside in an A_1 cluster orbital, and 4 in an E cluster orbital, so the orbital occupation is indeed $a_1^6 e^4$ with respect to the ground-state electronic configuration of the bare metal cluster. However, for several cases in Table III, especially for hollow-site coordination, the difference in orbital occupations between the ground-state [metal+CO] cluster and the ground-state bare cluster turns out instead to be $a_1^5 e^5$ or $a_1^4 e^6$. In order to make a straightforward comparison of the donation (A_1) and back-donation (E) contributions between the different binding geometries and metals, then, it is necessary to "fix" the orbital occupations for the bare cluster,

so to always obtain a $a_1^6 e^4$ difference in orbital occupation compared to the CO-coordinated cluster. This notion of referring to an excited state of the bare metal cluster is inspired by the "cluster bond preparation" approach of Siegbahn and Wahlgren.[40] A similar procedure was followed for NO, so to set the difference in orbital occupations between the bare and NO-coordinated clusters equal to the electronic configuration of free NO, $a_1^6 e^5$. The results of this analysis, expressed as A_1 and E orbital components of the zero-field binding energies for each system in atop and hollow sites, are summarized in Table V. The cases where the parameters refer to an "excited," rather than the lowest-energy (ground) state, are marked with an asterisk. While the "bond-prepared" E_b values are necessarily more negative than for the true ground state, the differences are mostly not large, ≈ 0.1–0.2 eV.

The magnitude of each of the major components of E_b, arising from steric, A_1 and E orbital interactions (Tables III–V), are seen to be sensitive to both the coordination site and the nature of the metal. One might expect that the metal–chemisorbate steric interaction, of which Pauli repulsion is dominant, would be larger in the hollow than the atop sites. Inspection of Tables III and IV, however, shows that the opposite is the case. This apparent anomaly is resolved by recognizing that the greater steric repulsion associated with hollow-site bonding is more than offset by a *decrease* in the intramolecular bond repulsion caused by greater C–O or N–O bond elongation in the hollow vs atop sites. (The bond expansion is clearly evident from the $r_{\text{C–O}}$ and $r_{\text{N–O}}$ values given in Tables III and IV, compared with those calculated for uncoordinated CO and NO, 1.139 and 1.166 Å, respectively.[20])

Indeed, this point is clarified by examining otherwise-similar DFT calculations for CO and NO binding where the $r_{\text{C–O}}$ and $r_{\text{N–O}}$ values remain *unchanged* upon chemisorption, so that the intramolecular steric-repulsion component is "constrained" upon forming the metal–chemisorbate bond, therefore enabling $E(\text{st})$ to reflect chiefly the effect of the latter.[41] Such "bond-constrained" binding parameters, with $r_{\text{C–O}}$ and $r_{\text{N–O}}$ remaining at their equilibrium *uncoordinated*
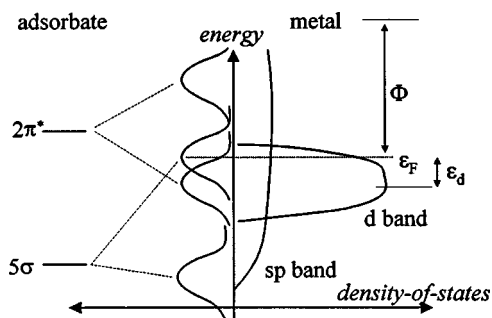
FIG. 1. Orbital energy-level diagram for metal–chemisorbate systems.

TABLE VI. Periodic d-band parameters for Pt-group metals.[a]

	Ru		Rh		Pd
n_d	0.7	n_d	0.8	n_d	0.9
ε_d/eV	−1.41	ε_d/eV	−1.73	ϵ_d/eV	−1.83
V^2_{ad}	3.9	V^2_{ad}	3.3	V^2_{ad}	2.8
Φ/eV		Φ/eV	5.6	Φ/eV	5.6

	Ir		Pt
n_d	0.8	n_d	0.9
ε_d/eV	−2.11	ε_d/eV	−2.25
V^2_{ad}	4.5	V^2_{ad}	3.9
Φ/eV	5.7	Φ/eV	5.9

[a]n_d is the idealized d band filling, ε_d is the center of the d band, V^2_{ad} is the adsorbate (s,p)–metal d band coupling matrix element squared (all three from Ref. 12), and Φ is the work function of the clean (111) surfaces (from Table I).

values in the chemisorbed state, are given for Pt/CO and Pt/NO in Ref. 20. Examples of E(st) values obtained by using this bond-constrained approach are also included (in parentheses) for the Pt/CO system in Table III. These values are seen to be markedly larger than the corresponding ''bond-relaxed'' values listed alongside, with the hollow site now yielding a *greater* M–CO steric repulsion. Such larger ''bond-constrained'' E(st) values in the hollow versus atop site were obtained for the other systems in Tables III and IV; the trend is consistent with conventional expectations derived from the behavior of monoatomic adsorbates. The *smaller* E(st) values for hollow versus atop binding obtained from the present ''equilibrium bond-length'' calculations seen in Tables III and IV are therefore identified clearly from the larger decrease in the *intramolecular* component upon binding in the former site, associated with greater bond elongation resulting from enhanced back-donation. Although the present DFT calculations for ''equilibrium-relaxed'' bond configurations are more realistic, the corresponding energetic parameters obtained for such ''intramolecular bond-constrained'' adsorption are clearly informative since they focus attention on the metal-chemisorbate bond *itself*.

Orbital interactions are expected to be more favorable on high-coordination sites when of bonding character and low-coordination sites when of predominately antibonding character. According to the classical Blyholder model,[42] the orbital interactions for CO and NO adsorbed on metal surfaces consist mainly of the 5σ donation and $2\pi^*$ back-donation contributions, as illustrated in Fig. 1. Both the 5σ donation and $2\pi^*$ levels split up into bonding and antibonding resonance due to their interaction with the localized d-band states, and broaden due to the interaction with the much more delocalized sp-band states. Since the 5σ state is low lying in energy (Fig. 1), its antibonding contribution can be minimized by binding in low-coordination sites. For the $2\pi^*$ level, on the other hand, the bonding resonance has a significant density-of-states near the Fermi level, whereas its antibonding resonance is usually of high energy so that it does not play a role. On this basis, the back-donation interaction should favor chemisorbate binding at high-coordination sites. Inspection of Table V shows that the back-donation interaction is indeed uniformly more favorable for a given metal/chemisorbate in the hollow vs the atop site. Conversely, the donation term is consistently more favorable for atop coordination (Table V), again in accord with conventional expectations.

The variations in the steric and orbital contributions to E_b between the five Pt-group surfaces (Tables III–V) can be understood most readily with reference to the metal d-band parameters, summarized in Table VI, which are taken in part from Ref. 12. Included are the idealized d-band filling, n_d, the center of the d band, ε_d, the metal work function, Φ, and the adsorbate–metal d band coupling-matrix element, V^2_{ad}. The last term is a measure of the adsorbate-metal d states overlap and hence the ''diffuseness'' of the metal d orbitals. Since the dominant factor in the steric repulsion should be mimicked by the orbital overlap factor V^2_{ad}, along with the d-band filling, one expects the steric repulsion to increase towards the lower-left corner of the Pt-group metals, as arranged in the Periodic Table. This is borne out by the results in Tables III and IV. The steric repulsions for CO on Ru, however, are somewhat smaller than on its right-hand neighbor Rh, which may reflect the lower d-band filling of Ru.

Following the Blyholder picture illustrated in Fig. 1, one expects the back-donation interaction to get stronger with higher d-band energies and fillings ε_d and n_d, favoring binding at high-coordination sites. On the other hand, the donation interaction is favored by lower d-band energies and fillings, so that adsorbate electrons can populate metal orbitals. Variations in the work function Φ between the metals should influence this picture; lower Φ values imply upward shifts in the Fermi level energy, increasing the back-donation into the $2\pi^*$ bonding resonance and thereby favoring multifold coordination. From the trends in the various metal parameters in Table VI, it is predicted that back-donation should become more favorable towards the upper-right corner of the Pt-group elements, whereas the donation term is expected to be stronger towards the lower-left corner.

Inspection of Tables III and IV reveals that the variations in the overall orbital and steric contributions to the surface bonds vary with the metal in a partly offsetting manner; these terms become less negative and positive, respectively, in moving from the bottom-left to the top-right corner of the Pt-group metals. (This trend correlates roughly with the metal-dependent variations in the d-orbital ''diffuseness,'' as expressed by V^2_{ad}, as might be expected, the larger steric and orbital terms tend to be associated with greater V^2_{ad} values.) Significantly, the orbital decomposition analysis

given in Table V not only confirms the qualitative metal-dependent bonding predictions anticipated from the Blyholder model along with the metal parameters in Table VI, but also furnishes more detailed insight. The favorable CO hollow-site binding on Pd is seen to be driven by the back-donation interaction along with the smaller net steric repulsion, combined with the relatively weak orbital interactions for the alternative atop geometry. The characteristically strong preference for atop CO binding on Ir clearly arises from the especially favorable A_1 donation term more than offsetting the relatively large steric repulsion on this metal. Interestingly, the exclusively atop CO coordination also observed on Ru is due partly to additional factors: while the donation interaction is favorable, the preference for atop vs hollow-site binding is driven partly by the back-donation term along with the relatively mild steric repulsion on this metal.

Inspection of Table V along with the overall steric and orbital energy components in Tables III and IV shows clearly that the greater propensity of NO vs CO for hollow-site binding arises primarily from the very strong back-donation interaction in this coordination geometry, undoubtedly associated with the lower energy of the $2\pi^*$ state on NO.[20] Another factor favoring hollow vs atop NO binding on Ru and Ir is the weaker net steric repulsion obtained in the former geometry (Table IV). [Similarly to CO, the smaller *net E*(st) term seen for hollow versus atop binding arises from the greater N–O bond expansion in the former geometry; ''bond-constrained'' calculations as considered above, so to ''fix'' the internal N–O steric repulsion component, yield again *larger E*(st) values in the multifold NO binding geometry.[41]] Note that the apparent preference of NO for atop binding on Ir(111) as gleaned from electrochemical IRAS (vide supra[6,8]) is therefore not mimicked by the DFT calculations (Table IV). In view of the uniform agreement between experiment and theory obtained for the other metal–chemisorbate combinations, the actual preferred binding site for Ir(111)/NO is apparently thereby regarded as uncertain at this juncture.

By and large, then, our DFT calculations provide a detailed rationale for the observed metal-dependent chemisorbate binding geometries at zero external field, namely the tendency to shift from preferred atop to hollow-site CO coordination towards the upper-right members of the Pt-group metals. The metal-dependent trends can be understood not only on the basis of the metal *d* parameters, but also from the orbital-energy decomposition into donation and back-donation contributions. The latter shows that the atop CO coordination preferred on Ir is due predominantly to strong chemisorbate–metal donation. The opposite, multifold-preferred, CO coordination on Pd arises from the mild yet relatively favorable back-donation interaction combined with the small steric repulsion for this metal.

2. Field-dependent binding energies

As noted at the outset, also of central interest in the present study is understanding the quantum-chemical factors responsible for the observed dependencies of the preferred binding-site geometries and vibrational frequencies on the surface potential and hence electrostatic field. In the interest

of brevity, we restrict attention here to field-dependent CO binding energetics. Figures 2(a)–2(c) show plots of the calculated binding energies, along with the separate steric, donation, and back-donation components vs the external field, $F(V/\text{Å}^{-1})$, on Pt, Ir, and Pd, respectively. The latter two metals are chosen in view of their propensity for atop and hollow-site CO binding, respectively, whereas the first exhibits a field-dependent binding preference, switching to multifold coordination at negative fields.[20] The orbital energy terms are plotted as differences from their zero-field values, so to circumvent the complication from variable electronic configurations noted above. Parameters for atop and hollow-site coordination are shown as open and filled circles, respectively. As outlined further below, the range of field strengths considered in Fig. 2, -0.5 to 0.5 V/Å, corresponds roughly to a span of $\Phi - \Phi(F=0)$ values of ± 1.5 eV, encompassing the potential range to which the electrochemical IRAS data in Table I refer to. For the most part, the available electrochemical IRAS data refer to negative $\Phi - \Phi(F=0)$ values, around -1 to 0 eV (Table I).

We consider first the archetypal Pt(111)/CO system [Fig. 2(a)]. In addition to the field-dependent binding-energy parameters extracted from the present ''equilibrium-relaxed'' C–O configurations, shown as solid lines, also included in Fig. 2(a) are corresponding calculations referring instead to a chemisorbed C–O bond length constrained at its *uncoordinated* value (dashed lines, as in Ref. 20). As discussed above, this ''bond-constrained'' tactic acts to ''fix'' the internal C–O steric repulsion, so that the E(st) values reflect chiefly the effects of surface-bond formation. A clear difference between the ''C–O relaxed'' and ''C–O constrained'' parameters is the opposite sign of the steric repulsion-field dependence. The increase in the steric term seen towards more negative fields in the latter case [Fig. 2(a)] is due to enhanced metal–CO repulsion as the electron density builds up on the metal surface. The accompanying increased occupation of sigma-type antibonding orbitals may also contribute to the greater Pauli repulsion. The opposite behavior seen in the ''bond-relaxed'' case is ascribed to a progressive decrease in the intramolecular steric repulsion as the C–O bond elongates towards more negative fields (see Table I of Ref. 20), more than offsetting the above effect.

Another significant difference concerns the field-dependent behavior of the hollow-site donation versus back-donation components. In the ''C–O constrained'' case, the increase in the back-donation interaction seen towards more negative fields are substantially larger than the opposite field dependence evident for the donation term. (The opposite signs in these terms is readily understood in terms of field-dependent metal-chemisorbate charge transfer.) The dominant field-dependent back-donation term also more than offsets the increased steric repulsion seen at more negative fields, thereby being solely responsible for the progressively more negative E_b values obtained under these conditions [Fig. 2(a)]. While the *overall* E_b-field behavior predicted for the ''C–O relaxed'' case is similar, the binding components exhibit quite different characteristics. Aside from the qualitatively different steric repulsion behavior already mentioned, the field-dependent back-donation and donation terms
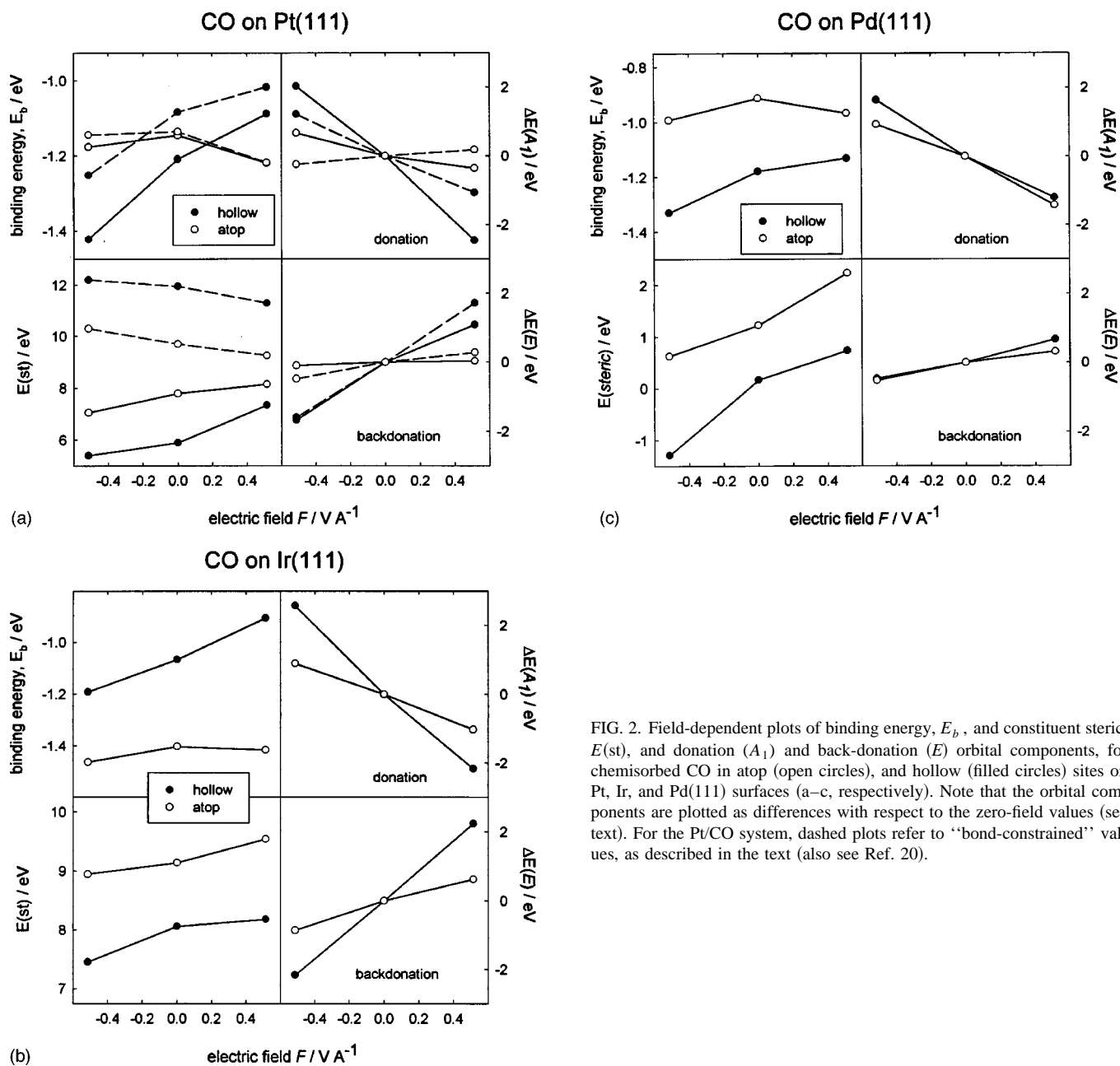
CO on Pt(111)

CO on Pd(111)

CO on Ir(111)

FIG. 2. Field-dependent plots of binding energy, E_b, and constituent steric, $E(\text{st})$, and donation (A_1) and back-donation (E) orbital components, for chemisorbed CO in atop (open circles), and hollow (filled circles) sites on Pt, Ir, and Pd(111) surfaces (a–c, respectively). Note that the orbital components are plotted as differences with respect to the zero-field values (see text). For the Pt/CO system, dashed plots refer to ''bond-constrained'' values, as described in the text (also see Ref. 20).

are now almost offsetting, so that the larger $-E_b$ values for hollow-site binding seen towards more negative fields are now due chiefly (albeit formally) to the steric repulsion term. The increased preference for hollow-site vs atop binding under these conditions is due partly to greater decreases in steric repulsion for the former geometry, ascribable to progressively increased C–O bond lengths. While these differences are in a sense subtle, they point to the need to consider variations in C–O as well as M–CO bonding when describing the field-dependent surface binding energetics. This issue will be discussed in more detail elsewhere.[43] Regardless of the details, multifold CO coordination is predicted to become more greatly stabilized by higher negative fields than atop binding, in accordance with experiment (Table I).

Turning now to iridium and palladium [Figs. 2(b) and 2(c)], by and large the field-dependent behavior of both E_b and its constituent parameters are comparable to that seen on

platinum. In each case, hollow-site coordination is stabilized increasingly towards more negative fields, usually to a greater extent than for atop binding, due partly to enhanced back-donation. However, the energetic preference for atop and hollow-site CO binding on Ir and Pd, respectively, is sufficiently large to be unaffected by field alterations, at least over the experimentally accessible range [Figs. 2(b) and 2(c)]. While data are not shown here, rhodium features near-equal atop and hollow-site E_b values at zero field (Table III), so that a switch to multifold binding is predicted at negative fields, similarly to platinum. These predictions are also in accordance with the electrochemical IRAS data (Table I).

Qualitatively similar factors control the field-dependent NO bonding energies, as outlined for Pt/NO in Ref. 20. As already alluded to, however, a major difference is that the $2\pi^*$ and 5σ levels of NO are 2–3 eV lower in energy than for CO, yielding stronger back donation and weak donation.

TABLE VII. Metal-dependent CO vibrational parameters.[a]

	Ru			Rh			Pd	
	Atop	Hollow		Atop	Hollow		Atop	Hollow
ν_{C-O}/cm^{-1}	1901	1648	ν_{C-O}/cm^{-1}	1950	1687	ν_{C-O}/cm^{-1}	2012	1795
$d\nu/dF$ cm^{-1} Å/V	115	148	$d\nu/dF$ cm^{-1} Å/V	89	146	$d\nu/dF$ cm^{-1} Å/V	117	174

				Ir			Pt	
				Atop	Hollow		Atop	Hollow
			ν_{C-O}/cm^{-1}	1975	1702	ν_{C-O}/cm^{-1}	1987	1714
			$d\nu/dF$ cm^{-1} Å/V	87	120	$d\nu/dF$ cm^{-1} Å/V	102	125

[a]ν_{CO} is the zero-field C–O vibrational frequency in atop and hollow sites (as indicated), and $d\nu/dF$ is the corresponding frequency-field slope at zero field.

As a consequence, NO is predicted to bind preferentially at the hollow site on all five metals throughout the range of external fields considered here, in reasonable accordance with experiment (Table I).

3. Intramolecular stretching frequencies

Tables VII and VIII summarize the results of field-dependent DFT calculations of intramolecular C–O and N–O frequencies on the five transition metals. For each metal–chemisorbate and binding-site combination, we list the calculated intramolecular stretching frequencies for CO and NO, ν_{CO} and ν_{NO}, respectively, at zero external field ($F=0$), along with the corresponding field dependencies, given as $d\nu/dF$ ($cm^{-1} V^{-1}$ Å) (Table VII and VIII, respectively). While the latter refer to the ν–F slope at $F=0$, in practice the $d\nu/dF$ values are insensitive to F (within $\approx 10\%$), at least for fields, $|F| \leq 0.5$ V Å^{-1}, of relevance to the electrochemical IRAS data considered here. For uncoordinated CO and NO, we calculate from DFT ν_{CO} and ν_{NO} values of 2095 and 1843 cm^{-1}; these are close to (yet slightly lower than) the experimental values of 2145 and 1877 cm^{-1}, respectively. The corresponding computed values of ($d\nu_{CO}/dF$) and ($d\nu_{NO}/dF$) for the uncoordinated molecules, 45 and 32 cm^{-1} V^{-1} Å, respectively, similar to earlier theoretical estimates,[44] are markedly smaller than for

the chemisorbed species (Tables VII and VIII), reflecting the major role of surface bonding in determining the latter quantities.

The equilibrium metal–chemisorbate and intramolecular chemisorbate bond distances (r_{M-C}, r_{M-N}, and r_{C-O}, r_{N-O}, respectively) at zero field, extracted as part of the vibrational calculations, are listed in Tables III and IV. The former values were obtained from the energy−r_{M-C}/r_{M-N} distance minima with r_{C-O} and r_{N-O} set at their uncoordinated values. These r_{M-C}, r_{M-N} values were then used to compute energy-bond distance profiles for the C–O and N–O bonds, yielding the zero-field r_{C-O} and r_{N-O} values for $F=0$ listed in Tables III and IV. The ν_{CO} and ν_{NO} values for $F=0$ given in Tables VII and VIII were obtained from these potential-energy profiles as noted above. Bond-frequency calculations as a function of F, yielding the ($d\nu_{CO}/dF$) and ($d\nu_{NO}/dF$) values (Tables VII and VIII, respectively) were undertaken in the same fashion. While adequate for the present purposes, this procedure is only approximate. We have also undertaken more precise calculations, involving iterative adjustment of the equilibrium r_{M-C} and r_{M-N} values for the alterations in r_{C-O} and r_{N-O} caused by surface bond formation. Fortunately, however, the results obtained by the present simplified route are acceptably close to those using the more complete analysis (ν and $d\nu/dF$ values within ≈ 20 cm^{-1} and 10%–20%, respectively). Related DFT results obtained with

TABLE VIII. Metal-dependent NO vibrational parameters.[a]

	Ru			Rh			Pd	
	Atop	Hollow		Atop	Hollow		Atop	Hollow
ν_{N-O}/cm^{-1}	1640	1403	ν_{N-O}/cm^{-1}	1680	1471	ν_{N-O}/cm^{-1}	1715	1547
$d\nu/dF$ cm^{-1} Å/V	118	154	$d\nu/dF$ cm^{-1} Å/V	184	160	$d\nu/dF$ cm^{-1} Å/V		170

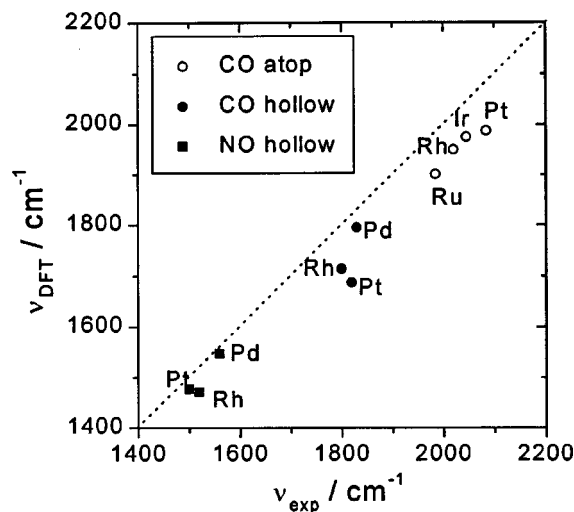|				Ir			Pt	
				Atop	Hollow		Atop	Hollow
			ν_{N-O}/cm^{-1}	1690	1452	ν_{N-O}/cm^{-1}	1702	1477
			$d\nu/dF$ cm^{-1} Å/V	174	163	$d\nu/dF$ cm^{-1} Å/V	155	159

[a]As in Table VII, except for N–O frequencies.

FIG. 3. Comparison between the intramolecular C–O and N–O chemisorbate frequencies at zero external field calculated by DFT, ν_{DFT}, and corresponding experimental values, ν_{exp}, referring to limitingly low coverages at metal–UHV interfaces (see text and Table II).

FIG. 4. Comparison of field-dependencies of ν_{CO} and ν_{NO} calculated by DFT, $d\nu_{DFT}/dF$, and observed quantities, $d\nu_{exp}/dF$, as extracted from experimental potential-based values by using Eq. (1) (see text and Table II).

a full optimization of r_{M-C}, r_{C-O} bond distances will be presented elsewhere in a study concerned with field-dependent metal-CO stretching frequencies.[43]

A comparison between the intramolecular chemisorbate frequencies at zero external field calculated here by DFT, $\nu_{DFT}(F=0)$, and the corresponding experimental values, $\nu_{exp}(F=0)$, is plotted in Fig. 3. The latter values, taken from Table II, refer to limitingly low coverages at the metal–UHV interfaces. [The experimental value for Ru(0001)/CO, 1985 cm^{-1}, is taken from Ref. 36.] As noted above, these ν(UHV) values are in most cases close to (within $\approx$20–30 cm^{-1} of) the corresponding electrochemical quantities ν(EC) evaluated at an equivalent surface potential. Figure 3 shows that the DFT and experimental frequencies are in very good agreement, the slightly (20–60 cm^{-1}) lower DFT values mimicking the systematically small (2%–3%) discrepancies between these quantities for uncoordinated CO and NO (vide supra). This excellent concordance gives us confidence in pursuing further analysis of the DFT results aimed at deciphering the major chemical bonding factors responsible for the observed metal-dependent behavior.

A comparison of the field dependencies of ν_{CO} and ν_{NO} calculated by DFT, expressed as $d\nu_{DFT}/dF$ values (taken from Tables VII and VIII), with the experimental behavior is plotted in Fig. 4. The latter quantities, $d\nu_{exp}/dF$, were extracted from the experimental potential-based values, $d\nu/dE$, at low CO or NO coverages given in (or estimated from) Table II, by using[4]

$$(d\nu/dF) = d_{dl}(d\nu/dE),   (1)$$

where d_{dl} is the effective thickness of the double-layer region that experiences alterations in the applied electrode potential. To a first approximation,[4] $d_{dl} \approx 3$ Å in the aqueous media employed for the experimental ($d\nu/dE$) data given in Table II. The $d\nu_{DFT}/dF$ values are seen to be in rough accordance with the $d\nu_{exp}/dF$ estimates, although the variations of the former tend to be less, and are $\approx$20%–40% smaller, than the
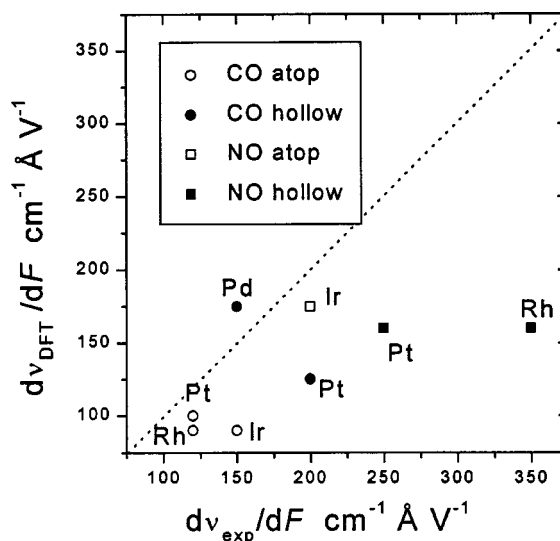
latter values. These discrepancies are probably due partly to the role of coadsorbed solvent in affecting the local electrostatic field sensed by the chemisorbate. Nonetheless, the larger $d\nu_{DFT}/dF$ values predicted for NO vs CO are in accordance with the experimental observations (Fig. 4, Table II).

Overall, then, the field-dependent intramolecular stretching frequencies by DFT cluster calculations are in reasonable agreement with the experimental observations, especially with regard to the metal-dependent frequencies (Fig. 3). Given this favorable situation, we can justifiably utilize DFT to disentangle the various contributions (steric, donation, and back-donation) to the field-dependent chemisorbate vibrational frequencies in a similar fashion to the above analysis of binding energies.[45] It is helpful to recall that the ν_{CO} and ν_{NO} frequencies refer to the shape of the potential energy-bond displacement well; we can therefore decompose these DFT-computed surfaces into the above components, which together approximately comprise the overall potential-energy well. A similar procedure has indeed been utilized by Bagus and Illas *et al.* to analyze the orbital components of the vibrational frequency shifts observed upon CO chemisorption.[46–49]

The following procedure was employed here. The vibrational potential-energy surface (PES) for the uncoordinated CO or NO, containing steric (electrostatic plus Pauli repulsion), and orbital overlap (A_1, E) contributions was first computed, along with the corresponding PES calculated for chemisorbed CO or NO. Next, for the uncoordinated molecule we replace the steric component of the PES with that calculated for the *chemisorbed* species. This generates a new PES, containing the effects of steric repulsion but *without* metal–chemisorbate orbital hybridization. The resulting chemisorbate vibrational frequencies are markedly blue-shifted, by $\approx$300–800 cm^{-1}, from the uncoordinated values. This effect has been noted previously by Bagus and Illas *et al.*,[46,48] and identified as a ''wall effect,'' whereby the

TABLE IX. Examples of decomposition of zero-field vibrational frequency shifts (cm^{-1}) for CO and NO chemisorption into steric and orbital contributions.[a]

System	Steric	Donation	Back-donation	Rest	Final
Ru–CO atop	+670	−349(−471)	−562(−440)	+47	1901
Rh–CO atop ($a_1^2 e^4 a_2^2$)	+737	−299(−467)	−650(−476)	+77	1960
Rh–CO atop ($a_2^2 a_2^2 e^2$)	+737	−304	−698	+109	1939
Rh–CO atop ($a_2^2 e^4 a_1^2$)	+737	−303	−638	+104	1995
Pd–CO atop	+307	−107(−165)	−406(−348)	+23	2012
Ir–CO atop	+877	−408(−634)	−664(−437)	+74	1975
Pt–CO atop	+743	−328(−486)	−569(−411)	+46	1987
Pt–CO hollow	+645	−198(−371)	−910(−737)	+82	1714
Pt–NO hollow	+580	−221(−406)	−835(−662)	+110	1477

[a]The far-left column is the cluster/binding site configuration (additional two entries for Rh/CO refer to excited-state configurations noted, see text). Adjacent three columns (steric/donation/back-donation) give the change in frequency (cm^{-1}) due to each contribution, calculated with respect to the uncoordinated DFT frequency of 2095 and 1843 cm^{-1} for CO and NO, respectively. The main entries have been calculated in the order as given in the table, i.e., steric-donation-back donation, whereas the entries within parentheses refer to the order steric-back donation-donation. The column ''rest'' refers to the residual frequency shift upon adsorption not accounted for by the sum of steric/donation/back-donation. The far-right column gives the coordinated C–O/N–O vibrational frequency.

metal surface acts to ''stiffen'' the motion of the lead-in (C, N) atom. In two further steps, we separately include the PES components for the chemisorbed molecule associated with A_1 and E orbital overlap.[50] Both these components act to markedly redshift the intramolecular chemisorbate frequency.

Table IX provides a representative summary of these ''separated'' steric, donation, and back-donation components at zero external field, $\Delta\nu$, primarily for chemisorbed CO. The three contributions added together differ slightly from the overall chemisorbate frequencies, listed in the far right-hand column. (This difference, labeled ''rest,'' listed in the adjacent column, is due to A_2 orbital and small correction terms.) The $\Delta\nu$ values for the donation and back-donation steps also depend on the order in which these terms are added to the chemisorbate PES; values referring to the reverse order (back-donation/donation) are given in parentheses in Table IX. An overall perusal of Table IX reveals that *both* the donation and back-donation components act to markedly redshift the chemisorbate frequency. The former result is at first sight surprising: removing an electron from the 5σ orbital for uncoordinated CO yields instead a marked (105 cm^{-1}) *blueshift*, as estimated from a spin-unrestricted DFT calculation. As pointed out by Illas *et al.*,[48] however, the opposite redshift associated with $5\sigma(A_1)$ donation for chemisorbed CO arises from a decrease in the C–O Pauli repulsion since the orbital electron density resides mainly on the C atom. Nevertheless, as might be anticipated, Table IX shows that the predominant contribution to the net frequency redshift upon chemisorption arises from the back-donation component.

We now examine the origins of the periodic trends in zero-field chemisorbate frequencies in terms of this decomposition analysis. The DFT ν_{CO} (and ν_{NO}) values within a given binding site are seen to increase monotonically from left to right in the $5d$ (Ir, Pt) and especially the $4d$ (Ru, Rh, Pd) series (Tables VII and VIII), a finding which is in accordance with experiment (Table I). Inspection of Table IX, however, shows that there is no *single* contribution

which is responsible for this overriding Periodic trend. Nevertheless, the donation redshift component does become progressively smaller from Ru to Pd, and from Ir to Pt, increased d-band filling roughly accounting for the trend. However, there are substantial offsetting $\Delta\nu$ contributions from both steric and back-donation, so that the overall bond-frequency trends for the $4d$ series are due to a subtle interplay of all three factors, at least according to this simplified analysis. Also included in Table IX are calculations for atop Rh/CO in three different, close-lying, electronic states, with the HOMO configurations a_2^2, e^2, and a_1^2 (the first being the ground state). The similarity in the decomposed $\Delta\nu$ terms, even though the overall ν_{CO} values differ, gives us further confidence in the applicability of the procedure.

The field-dependent DFT frequencies can also be analyzed using a similar procedure. We take as a ''reference state'' the chemisorbate at a negative field ($F = -0.514$ V Å$^{-1} \equiv -0.01$ a.u.). We then add sequentially to the negative-field PES steric, donation, and back-donation components calculated for an equal *positive* electrostatic field, thereby estimating their separate contributions to the field-dependent chemisorbate frequencies from -0.514 to 0.514 V Å^{-1}. Representative $\Delta\nu/\Delta F$ components obtained in this manner are listed in Table X. (As in Table IX, the donation and back-donation components obtained by including them in the reverse order are given in parentheses, and the ''rest'' column again refers to the residual differences between the overall $\Delta\nu$ values and the sum of the components when included sequentially.)

The steric and donation contributions are seen to usually be negative. The former $\Delta\nu/\Delta F$ component likely arises from the lower metal surface electron density towards positive fields, diminishing the extent of steric repulsion with the chemisorbate electrons and hence yielding a shallower PES. The negative $\Delta\nu/\Delta F$ component from electron donation is also readily understandable given that this orbital interaction should lessen towards more positive fields. The small absolute values of the latter, however, signal an interesting insen-

TABLE X. Examples of decomposition of frequency-field vibrational frequency shifts (cm^{-1}).[a]

System	Steric	Donation	Back-donation	Rest	Overall
Ru–CO atop	−197	+34 (+22)	+336(+348)	−56	+117
Ru–CO hollow	−60	−43 (−36)	+249(+242)	+6	+152
Rh–CO atop	−185	−109 (−87)	+389(+355)	−2	+91
Pd–CO atop	−103	−60 (−39)	+246(+225)	+36	+119
Pd–CO hollow	−131	−14 (−26)	+268(+280)	+37	+157
Pd–NO hollow	−55	−5 (−26)	+276(+297)	−46	+170
Pt–CO atop	−131	−7 (−6)	+264(+263)	−16	+110
Pt–CO hollow	−72	−20 (−21)	+201(+202)	+22	+131
Pt–NO atop	−45	−100 (−93)	+360(+353)	−93	+172
Pt–NO hollow	+27	−67 (−69)	+193(+195)	+16	+169

[a]The far-left column is the cluster/binding site configuration. The far-right column is the overall frequency increase (cm^{-1}) computed for a change in the applied field from $F = -0.514$ V/Å to $F = +0.514$ V/Å. The middle three columns (steric/donation/back-donation) give the corresponding field-induced frequency shift due to each contribution. The main entries have been calculated in the order as given in the table, i.e., steric-donation-back donation, whereas the entries within parentheses refer to the order steric-back donation-donation. The column ''rest'' refers to the residual field-induced frequency shift not accounted for by the sum of these components (cf. Table IX).

sitivity of the donation interaction to the electrostatic field; a similar result was noted in a recent DFT study of the Pt(100)/CO system.[19(b)] Significantly, the dominant contribution to the field-dependent chemisorbate frequencies is provided by the back-donation term (Table X). This large positive $\Delta\nu/\Delta F$ component easily outweighs the smaller negative steric and donation terms, accounting for the uniformly positive Stark-tuning slopes for CO and NO (Table II). The positive overall $\Delta\nu/\Delta F$ values are therefore clearly due to sharply diminished $2\pi^*$ back donation as the field, and hence the surface potential, becomes less negative/more positive.

However, scrutiny of the variations in the back-donation component with the nature of the metal, and for hollow versus atop coordination on a given metal, do not uncover any overriding trends as responsible for the observed variations in the Stark-tuning slopes. Thus the larger dν/dE slopes observed for CO bound in hollow versus atop sites (Table II) are apparently not associated with greater back-donation components, but rather from *smaller* back-donation terms being more than offset by less negative steric $\Delta\nu/\Delta F$ contributions (Table X). Evidently, then, the initiatively simple notion that the more positive Stark-tuning slopes typically observed for multifold coordinated CO are associated with greater field-dependent back-donation is not borne out by the present frequency-decomposition analysis. Rather, the overall picture that emerges is one that invokes the offsetting influences of two or more components on the overall field-dependent behavior. To some extent, this pattern reflects that seen above in the DFT analysis of the ν_{CO} and ν_{NO} shifts upon chemisorption at zero external field.

IV. CONCLUSIONS

Even though the present cluster-based calculations limit the analysis to atop and hollow-site binding at low coverage, it is evident that DFT provides an invaluable means of quantitatively deconvolving as well as describing the quantum-chemical factors responsible for the observed field-dependent binding geometries and vibrational properties for these benchmark metal–chemisorbate systems. While the metal– as well as electrode potential-dependent trends in the CO binding sites are consistent with expectations based on 5σ donation and $2\pi^*$ back-donation in the conventional Blyholder model, the DFT results furnish substantially more detailed insight into the roles of these orbital interactions, along with other (Pauli, electrostatic repulsion) components.

The decreasing propensity for atop vs multifold CO coordination observed in both electrochemical and UHV-based systems in moving from the lower-left to the upper-right Periodic corner of the Pt-group metals is due to an interplay between several factors. The orbital interactions, especially the donation component, increase towards the left-hand corner, thereby yielding uniformly preferred atop CO binding on iridium. While the orbital interactions weaken towards the upper-right corner, the steric repulsion also diminishes; the relatively favorable back-donation and steric terms drive the preferred hollow-site coordination on palladium. These metal-dependent variations in the DFT interaction terms can be understood with reference to the metal *d*-band parameters. Thus the lower band energies and band filling for iridium facilitate donation interactions, whereas the higher values for palladium encourage back-donation; the decreasing steric repulsion from Ir to Pd (along with weakened orbital interactions) is consistent with the diminishing ''diffuseness'' of the metal *d* orbitals. The markedly greater (indeed uniform) preference for hollow-site NO binding, as evident in the stronger back-donation and weaker donation interaction terms compared with CO, is readily accounted for by the lower $2\pi^*$ and 5σ energy levels of the former chemisorbate.

The uniformly excellent concordance seen between the calculated ν_{CO} and ν_{NO} frequencies and the experimental values at zero external field gives us considerable confidence in utilizing DFT to uncover the quantum-chemical factors behind the observed chemisorbate vibrational properties. Decomposing the overall adsorption-induced frequency shifts into steric, donation, and back-donation terms, undertaken in analogous fashion to the binding-energy analysis, shows that both orbital components contribute to the observed marked

redshifts. The observed differences in vibrational frequency with the metal surface, however, are due to a subtle interplay between all three interaction components. In particular, the progressive blueshift in the atop ν_{CO} frequency seen towards the right of the Pt-group series is not due primarily to back-donation effects. Nevertheless, the uniformly positive Stark-tuning slopes observed for chemisorbed CO and NO indeed arise predominantly from diminished back-donation towards more positive fields, in harmony with conventional wisdom. However, the observed variations in the Stark-tuning slope with the coordination geometry, metal, and the chemisorbate again cannot be ascribed primarily to the role of a single interaction term, but rather to a subtle interplay between several components.

In closing, then, DFT clearly offers considerable utility as a means of elucidating Periodic and related chemical trends in the vibrational properties of chemisorbates in potential-dependent electrochemical, as well as UHV environments. Further studies along these lines, including a detailed field-dependent analysis of metal–chemisorbate vibrational properties, will be reported in the near future.

ACKNOWLEDGMENTS

[1] For reviews, see (a) R. J. Nichols, in *Adsorption of Molecules at Electrodes*, edited by J. Lipkowski and P. N. Ross (VCH, New York, 1992), Chap. 7; (b) C. Korzeniewski and M. W. Severson, Spectrochim. Acta A **51**, 499 (1995); (c) T. Iwasita and F. C. Nart, Prog. Surf. Sci. **55**, 271 (1997); (d) M. J. Weaver and S. Zou, in *Spectroscopy for Surface Science*, Advances in Spectroscopy, Vol. 26, edited by R. J. H. Clark and R. E. Hester (Wiley, Chichester, 1998), Chap. 5.

[2] (a) S.-C. Chang and M. J. Weaver, J. Phys. Chem. **95**, 5391 (1991); (b) S-C. Chang and M. J. Weaver, Surf. Sci. **238**, 142 (1990); (c) S.-C. Chang and M. J. Weaver, J. Chem. Phys. **92**, 4582 (1990).

[3] (a) S.-C. Chang, X. Jiang, J. D. Roth, and M. J. Weaver, J. Phys. Chem. **95**, 5378 (1991); (b) X. Jiang and M. J. Weaver, Surf. Sci. **275**, 237 (1992).

[4] M. J. Weaver, Appl. Surf. Sci. **67**, 147 (1993).

[5] (a) S.-L. Yau, X. Gao, S.-C. Chang, B. C. Schardt, and M. J. Weaver, J. Am. Chem. Soc. **113**, 6049 (1991); (b) I. Villegas and M. J. Weaver, J. Chem. Phys. **101**, 1648 (1994); (c) S. Zou and M. J. Weaver, Surf. Sci. **446**, L95 (2000).

[6] C. Tang, S. Zou, M. W. Severson, and M. J. Weaver, J. Phys. Chem. B **102**, 8796 (1998).

[7] (a) C. Tang, S. Zou, and M. J. Weaver, Surf. Sci. **412/413**, 344 (1998); (b) C. Tang, S. Zou, M. W. Severson, and M. J. Weaver, J. Phys. Chem. B **102**, 8546 (1998); (c) C. Tang, S. Zou, S-C. Chang, and M. J. Weaver, J. Electroanal. Chem. **467**, 92 (1999).

[8] (a) M. J. Weaver, S. Zou, and C. Tang, J. Chem. Phys. **111**, 368 (1999); (b) M. J. Weaver, Surf. Sci. **437**, 215 (1999).

[9] (a) I. Villegas and M. J. Weaver, J. Phys. Chem. B **101**, 5842 (1997); (b) I. Villegas, R. Gomez, and M. J. Weaver, J. Phys. Chem. **99**, 14832 (1995).

[10] N. Kizhakevariam, I. Villegas, and M. J. Weaver, J. Phys. Chem. **99**, 7677 (1995).

[11] R. A. van Santen and M. Neurock, Catal. Rev. Sci. Eng. **37**, 557 (1995).

[12] (a) B. Hammer and J. K. Nørskov, in *Chemisorption and Reactivity on Supported Clusters and Thin Films*, NATO ASI Series, edited by R. M. Lambert and G. Pacchioni (Kluwer Academic, Dordrecht, 1997), Vol. 331, p. 285; (b) A. Ruban, B. Hammer, C. Stoltze, H. L. Skriver, and J. K. Nørskov, J. Mol. Catal. A: Chem. **115**, 421 (1997); (c) B. Hammer, Y. Morikawa, and J. K. Nørskov, Phys. Rev. Lett. **76**, 2141 (1996).

[13] (a) D. Loffreda, D. Simon, and P. Sautet, J. Chem. Phys. **108**, 6447 (1998); (b) D. Loffreda, D. Simon, and P. Sautet, Chem. Phys. Lett. **291**, 15 (1998); (c) Q. Ge and D. A. King, *ibid.* **285**, 15 (1998).

[14] (a) D. Loffreda, D. Simon, and P. Sautet, Surf. Sci. **425**, 68 (1999); (b) A. Eichler and J. Hafner, J. Chem. Phys. **109**, 5585 (1998).

[15] S. Holloway and J. K. Nørskov, J. Electroanal. Chem. **161**, 193 (1984).

[16] P. S. Bagus, C. J. Nelin, W. Müller, M. R. Philpott, and H. Seki, Phys. Rev. Lett. **58**, 559 (1987).

[17] (a) N. K. Ray and A. B. Anderson, J. Phys. Chem. **86**, 4851 (1982); (b) A. B. Anderson and M. K. Awad, J. Am. Chem. Soc. **107**, 7854 (1985); (c) S. P. Mehandru and A. B. Anderson, J. Phys. Chem. **93**, 2044 (1989).

[18] M. Head-Gordon and J. C. Tully, Chem. Phys. **175**, 37 (1993).

[19] (a) F. Illas, F. Mele, D. Curulla, A. Clotet, and J. M. Ricart, Electrochim. Acta **44**, 1213 (1998); (b) D. Curulla, A. Clotet, J. M. Ricart, and F. Illas, *ibid.* **45**, 639 (1999).

[20] M. T. M. Koper and R. A. van Santen, J. Electroanal. Chem. **474**, 64 (1999).

[21] (a) A. de Koster, A. P. J. Jansen, R. A. van Santen, and J. J. C. Geerlings, Faraday Discuss. Chem. Soc. **87**, 263 (1989); (b) A. Goursot, I. Papai, and D. R. Salahub, J. Am. Chem. Soc. **14**, 7452 (1992); (c) G. Pacchioni, S.-C. Chung, S. Krüger, and N. Rösch, Surf. Sci. **392**, 173 (1997).

[22] Amsterdam Density Functional Package, ADF 2.3.0, Department of Theoretical Chemistry, Vrije Universiteit, Amsterdam, 1997.

[23] E. J. Baerends, D. E. Ellis, and P. Ros, Chem. Phys. **2**, 41 (1973).

[24] G. te Velde and E. J. Baerends, J. Comput. Phys. **99**, 84 (1992).

[25] F. Jensen, *Introduction to Computational Chemistry* (Wiley, Chichester, 1999).

[26] S. H. Vosko, L. Wilk, and M. Nusair, Can. J. Phys. **58**, 1200 (1980).

[27] (a) A. D. Becke, Phys. Rev. A **38**, 3098 (1988); ACS Symp. Ser. **394**, 165 (1989); (c) J. P. Perdew, Phys. Rev. B **33**, 8822 (1986).

[28] E. L. Meijer, R. A. van Santen, and A. P. J. Jansen, J. Phys. Chem. **100**, 9282 (1996).

[29] For example: (a) M. C. Asensio, D. P. Woodruff, A. W. Robinson, K-M. Schindler, P. Gardner, D. Ricken, A. M. Bradshaw, J. C. Conesa, and A. R. Gonzalez-Elipe, Chem. Phys. Lett. **192**, 259 (1992); (b) T. Giessel, O. Schaff, C. J. Hirschmagl, V. Fernandez, K-M. Schindler, A. Theobald, S. Bao, R. Lindsey, W. Berndt, A. M. Bradshaw, C. Baddeley, A. F. Lee, R. M. Lambert, and D. P. Woodruff, Surf. Sci. **406**, 90 (1998); (c) N. Materer, A. Barbieri, U. Gardin, U. Starke, J. D. Batteas, M. A. Van Hove, and G. A. Somorjai, *ibid.* **303**, 319 (1994).

[30] M. Gierer, A. Barbieri, M. A. Van Hove, and G. A. Somorjai, Surf. Sci. **391**, 176 (1997).

[31] Y. J. Kim, S. Theruthasan, G. S. Herman, C. H. E. Peden, S. A. Chambers, D. N. Belton, and H. Permana, Surf. Sci. **359**, 269 (1996).

[32] S. Zou, R. Gomez, and M. J. Weaver, J. Electroanal. Chem. **474**, 155 (1999).

[33] (a) E. Schweizer, B. N. J. Persson, M. Tushaus, D. Hoge, and A. M. Bradshaw, Surf. Sci. **213**, 49 (1989); (b) M. Tushaus, E. Schweizer, P. Hollins, and A. M. Bradshaw, J. Electron Spectrosc. Relat. Phenom. **44**, 305 (1987).

[34] A. Rodes, R. Gomez, J. M. Feliu, and M. J. Weaver, Langmuir **16**, 811 (2000).

[35] F. Esch, Th. Greher, S. Kennon, A. Siokou, S. Ladas, and R. Imbihl, Catal. Lett. **38**, 165 (1996).

[36] F. M. Hoffmann, Surf. Sci. Rep. **3**, 107 (1983).

[37] (a) P. H. T. Philipsen, E. van Lenthe, J. G. Snijders, and E. J. Baerends, Phys. Rev. B **56**, 13556 (1997); (b) K. Bleakley and P. Hu, J. Am. Chem. Soc. **121**, 7644 (1999).

[38] For example, J. B. Benzinger, in *Metal–Surface Energetics*, edited by E. Shustorovich (VCH, New York, 1991), Chap. 2.

[39] B. Hammer, L. B. Hansen, and J. K. Nørskov, Phys. Rev. B **59**, 7413 (1999).

[40] P. E. M. Siegbahn and U. Wahlgren, in Ref. 38, Chap. 1.

[41] We have also calculated such ''bond-constrained'' $E(st)$ values by adjusting the bond lengths for the uncoordinated (gas-phase) species so to match the field-dependent equilibrium values for the chemisorbates. This alternative approach therefore adjusts the (internal) steric repulsion in the isolated species to match that for the chemisorbate, rather than vice versa. Interestingly, the $E(st)$ values obtained with either of the ''bond-constrained'' approaches are comparable (chiefly within 0.5 eV). This supports the notion that at least an approximate distinction can be made between steric-repulsion components associated with the internal chemisorbate, and metal–chemisorbate bonds.

[42] G. Blyholder, J. Phys. Chem. **68**, 2772 (1964).

[43] S. A. Wasileski, M. T. M. Koper, and M. J. Weaver (in preparation).

[44] (a) D. K. Lambert, Electrochim. Acta **41**, 623 (1996); (b) D. K. Lambert, Solid State Commun. **51**, 297 (1984).

[45] (a) T. Ziegler and A. Rauk, Theor. Chim. Acta **46**, 1 (1977); (b) K. Morokuma, Acc. Chem. Res. **10**, 294 (1977); (c) D. Post and E. J. Baerends, J. Chem. Phys. **78**, 5663 (1983); (d) F. M. Bickelhaupt, N. M. M. Nibbering, E. M. van Wezenbeek, and E. J. Baerends, J. Phys. Chem. **96**, 4864 (1992).

[46] P. S. Bagus and G. Pacchioni, Surf. Sci. **236**, 233 (1990).

[47] (a) P. S. Bagus, K. Hermann, and C. W. Bauschlicher, Jr., J. Chem. Phys. **80**, 4378 (1984); (b) P. S. Bagus and F. Illas, *ibid.* **96**, 8962 (1992).

[48] F. Illas, S. Zurita, A. M. Márquez, and J. Rubio, Surf. Sci. **376**, 279 (1997).

[49] A. M. Márquez, N. Lopez, M. García-Hernández, and F. Illas, Surf. Sci. **442**, 463 (1999).

[50] This differs from the (CSOV) analysis of Bagus *et al.* (Ref. 47) in which the subset of the full orbital space in which the orbitals are allowed to vary, and hence constitute a particular contribution, corresponding to the (virtual) orbital space of the fragments, whereas in the ADF analysis they refer to the (virtual) orbital spaces of the irreducible representations of the system's symmetry group.